Supplementary Material for:

Biomass-burning derived particles from a wide variety of fuels: Part 1: Properties of primary particles

Crystal D. McClure[1], Christopher Y. Lim[2,%], David H. Hagan[2], Jesse H. Kroll[2], Christopher D. Cappa[1,3,*]

[1] Department of Civil and Environmental Engineering, University of California, Davis, CA 95616

[2] Department of Civil and Environmental Engineering, Massachusetts Institute of Technology, Cambridge, MA, USA

[3] Atmospheric Sciences Graduate Group, University of California, Davis, CA, USA 95616

[%] Now at Department of Chemistry, University of Toronto, Ontario, Canada

[*] To whom correspondence should be addressed: cdcappa@ucdavis.edu

Description of Instrumentation

Particle Optical Property Measurements

Particle optical properties for PM_1 were measured at 405 nm and 532 nm using the UC Davis Cavity Ringdown-Photoacoustic Spectrometer (CRD-PAS). In the UC Davis CRD-PAS, Light absorption coefficients (b_{abs}; units = Mm^{-1}) for dry particles are determined using photoacoustic spectroscopy (Lack et al., 2012b). Light extinction coefficients (b_{ext}; units = Mm^{-1}) for dry (<20% relative humidity) particles are measured at 405 nm and 532 nm via cavity ringdown spectroscopy (Langridge et al., 2011). Humidified light extinction measurements (RH ~85%) are also measured at 532 nm by cavity ringdown spectroscopy. The absorption measurements from the PAS were calibrated relative to the extinction measurement from the CRD using gas-phase O_3 and NO_2 with an estimated accuracy of 5% at 532 nm and 8% at 405 nm. Light absorption and scattering coefficients were also measured at 781 nm using a commercial PASS-3 photoacoustic spectrometer (DMT, Inc.). In the PASS-3, light absorption coefficients are measured by photoacoustic spectroscopy. Light scattering coefficients (b_{sca}; units = Mm^{-1}) are determined for dry particles with the PASS-3 using reciprocal nephelometry. The absorption measured by the

PASS-3 was calibrated relative to the UC Davis PAS using polydisperse fullerene soot and assuming that the absorption Ångstrom exponent was 1.4 (Metcalf et al., 2013). The estimated uncertainty in b_{abs} at 781 nm is 10%.

Particle Composition Measurements

Refractory black carbon measurement

Refractory black carbon (rBC) concentrations and BC-specific particle size distributions were measured using a single particle soot photometer (SP2). The SP2 measures the concentration of rBC within individual rBC-containing particles. Sampled particles pass through a 1064 nm intracavity laser. Absorption of this light by rBC leads to rapid heating of the particles. If heating outweighs conductive cooling the particles will reach a sufficiently high temperature (i.e. their boiling point) that they will incandesce. The intensity of this incandescent light is proportional to the rBC mass of that particle (usually on the order of 0.1 – 10 fg per particle). Size distributions of only the rBC (exclusive of any other internally mixed material) are generated by converting the per particle mass to a volume equivalent diameter ($d_{p,VED}$ here, assuming ρ_{rBC} = 1.8 g cm^{-3}) and binning the particles by size. The SP2 was calibrated using size-selected fullerene particles (Lot L20W054, Alfa Aesar, Ward Hill, MA, USA).

When the number concentration of rBC-containing or non-rBC-containing particles is large, the SP2 may suffer from negative biases in the concentration measurement. This can happen when the SP2 detectors are triggered by one particle and a second passes through the viewing volume during the detection window (typically ~50 μs). Such particle coincidence effects can be minimized by decreasing the sample flowrate into the SP2 to decrease the likelihood that two particles are simultaneously in the viewing volume. Here, the SP2 sample flowrate was varied from 5 sccm to 120 sccm in a step-wise manner over the course of an experiment to deal with the very large dynamic range of concentrations in the mini chamber. The flow rate was increased to maintain an approximately constant particle count rate in the instrument while minimizing the influence of particle coincidence. Inspection of individual particle detection events indicates that particle coincidence was generally avoided.

The SP2 data were processed using the SP2 Toolkit from the Paul Scherer Institute (PSI), developed by Martin Gysel. The SP2 size-dependent counting efficiency was determined by

simultaneously measuring the concentration of the calibration particles with a mixing condensation particle counter (BMI Model 2002). The particle counting efficiency was found to be unity for particles with $d_{p,VED} > 100$ nm. The SP2 used in this study measured particles over the size range $90 \leq d_{p,VED} \leq 822$. Below the lower size limit, the detection efficiency falls off rapidly due, in part, to the large surface area-to-volume (SA-to-V) ratio of these particles. When the SA-to-V ratio is sufficiently large conductive cooling competes effectively with the radiative heating from the laser and the particles do not emit enough incandescent light at short enough wavelengths to trigger detection. Above the upper size limit, the incandescence level is sufficient to saturate the detector, leading to an underestimate in particle mass. All SP2 mass concentration measurements were corrected for the missing mass contained in particles below the lower and upper size limit, using a multi-mode fitting approach.

The observed campaign average distribution mode peak is around 150 nm. The observed distributions (1 min averages) were fit to a four-mode log-normal distribution to estimate and correct for the rBC outside of the SP2 detection window, i.e. for rBC "missing mass". The average ratio between the observed rBC concentration and the total estimated from fitting was 0.83 ± 0.06 (1σ). There was some experiment-to-experiment and time-dependent variability in the missing mass fraction that is accounted for by fitting the observations at 1 min time resolution. This approach follows that of Zhang et al. (2016). While a single mode fit provides a reasonably representation of the overall campaign average distribution, inspection of the individual distributions across the experiments indicates that a multi-mode fitting approach provides a substantially more robust description of the observed size distribution, especially as particle aging proceeds.

Composition and concentration of NR-PM

The concentration of non-refractory particulate matter (NR-PM) species in PM_1 were measured using a high-resolution time-of-flight aerosol mass spectrometer (HR-ToF-AMS, henceforth HR-AMS) (Canagaratna et al., 2007) during both the Fresno and Fontana studies, as discussed in detail by (Lim et al., 2019). The NR-PM components are functionally defined as those materials that evaporate rapidly after impaction onto a heated surface *in vacuo* at ~600 °C. The NR-PM components characterized include particulate sulfate, nitrate, ammonium, chloride and organic matter. The data were processed using the PIKA toolkit in IGOR (Wavemetrics, Inc.). The

collection efficiency (CE) of the HR-AMS was determined by comparison with size distributions measured using the scanning electrical mobility spectrometer (SEMS). The collection efficiency differed between primary and secondary and secondary particles and was found to co-vary with the volatility of the organic aerosol. The variation in the CE was empirically accounted for, as discussed in (Lim et al., 2019). The estimated uncertainty for the HR-AMS measurements is ±30%, although the precision is much better than this.

Particulate nitrated organics characterization

The concentration of nitrated organic functional groups (ON_f) is determined from the HR-AMS measurements. Kiendler-Scharr et al. (2016) showed that the fraction of total nitrate measured by the HR-AMS that derives from organic nitrate functional groups ($f_{ON\text{-}N}$) relates to the measured $[NO_2^+]/[NO^+]$ ratio (R_{meas}):

$$f_{ON-N} = \frac{(1+R_{ON})\cdot(R_{meas}-R_{calib})}{(1+R_{meas})\cdot(R_{ON}-R_{calib})} \quad \text{(S1)}$$

where R_{ON} = 0.1 and R_{calib} is an instrument-specific factor determined from calibration with NH_4NO_3 and here equaling 0.45. The Kiendler-Scharr et al. (2016) approach focused on the behavior of organic nitrates. We assume here that nitro-organics behave similarly and thus that ON_f encompasses contributions from both nitrate and nitro functional groups. Equation S1 is thought reliable when the $f_{ON\text{-}N} > 0.15$ (Bruns et al., 2010). The average $f_{ON\text{-}N}$ for the FIREX measurements is 0.74 ± 0.24 (1σ). The concentration of particulate ON functional groups is then $[ON_f] = f_{ON\text{-}N}\cdot[NO_3^-]$. Note that this includes only the mass of the functional group; the total mass concentration of the ON species (including the carbon backbone) can be estimated by multiplying the ON_f concentration by the ratio between an assumed MW for the ON species and that for the nitrate functional group. We assume that ON species have a MW = 200 amu, and thus $[ON] = 3.22\cdot[ON_f]$. If the ON signal is dominated by nitro functional groups, rather than nitrate, then the estimated [ON] is a lower limit.

Composition and concentration of BC-containing particles

The concentrations and composition of only BC-containing particles were determined using a soot particle aerosol mass spectrometer (SP-AMS) (Onasch et al., 2012). In the SP-AMS, a focused particle beam is intersected with an intra-cavity Nd:YAG laser operating at 1064 nm. Particles

containing BC are rapidly heated by the laser, leading to evaporation of both the NR-PM materials and the refractory BC. In these studies, the standard HR-AMS tungsten vaporizer was removed so that particles that do not contain BC are not vaporized and are therefore not detected. Thus, the SP-AMS is specific to BC-containing particles, as operated here. In addition to BC, the SP-AMS measures the internally mixed particulate inorganic (sulfate, nitrate, ammonium, and chloride) and organic mass loading. The NR-PM species that are associated with BC will be distinguished from the bulk average NR-PM species (from the HR-AMS) using the subscript BC (i.e. NR-PM_{rBC}). The SP-AMS particle detection efficiency is determined in large part by the extent of overlap between the particle and laser beam. Particles were sampled through a PM_1 aerodynamic lens, with particles measured down to ~40 nm vacuum aerodynamic diameter. The SP-AMS detection efficiency was determined by referencing the rBC concentration measured by the SP-AMS to that measured by the SP2, as in (Collier et al., 2018). The SP-AMS/SP2 ratio depended on the ratio between the NR-PM_{BC} and BC, with the NR-PM/rBC ratio decreasing as the SP-AMS/SP2 ratio increases. However, throughout this work we use only the [NR-PM_{rBC}]/[rBC] or [OA_{rBC}]/[rBC] ratios, which are not dependent on the absolute instrument calibration, but only the relative detection efficiency of these species. The coating-to-core mass ratio for both campaigns is calculated directly from the SP-AMS measurements as R_{BC} = [NR-PM]$_{BC}$/[BC].

Gas Composition Measurements

The concentrations of select gas-phase non-methane organic gases (NMOG) and some inorganic species (e.g. HONO) were measured using H_3O^+ and I^- chemical ionization mass spectrometers (CIMS), that included high-resolution time-of-flight mass spectrometers. Only the measurements from the PTR-TOF-MS, operated by the National Oceanic and Atmospheric Administration, are used here. The PTR-TOF-MS measurements are described in detail in (Koss et al., 2018) and (Sekimoto et al., 2018). In addition to the NMOG measurements, other inorganic gases (O_3, CO, CO_2, SO_2) were measured using commercial instrumentation.

Supplemental Figures & Tables

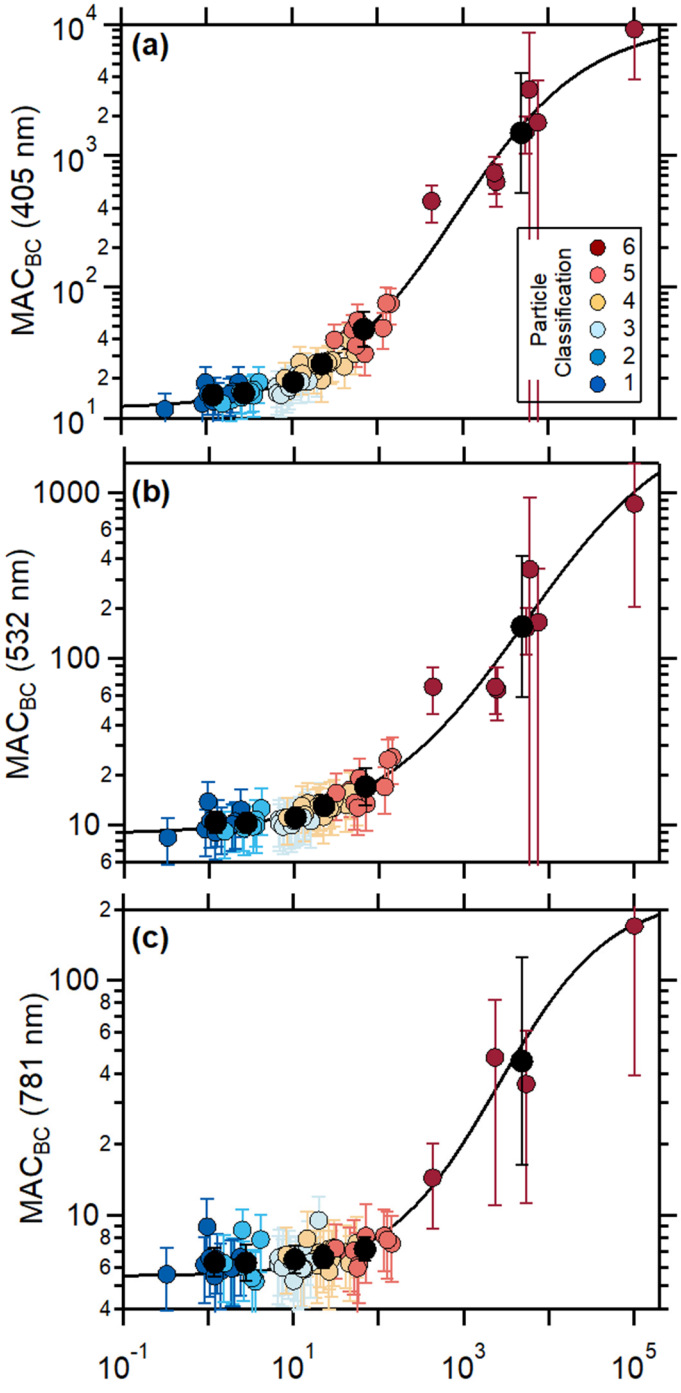

Figure S1. Relationship between the observed ambient particle *MAC*$_{BC}$ and the total particle [OA]/[rBC] at (a) 405 nm, (b) 532 nm, and (c) 781 nm. Individual points colored by Class (see text) and class averages as black circles.

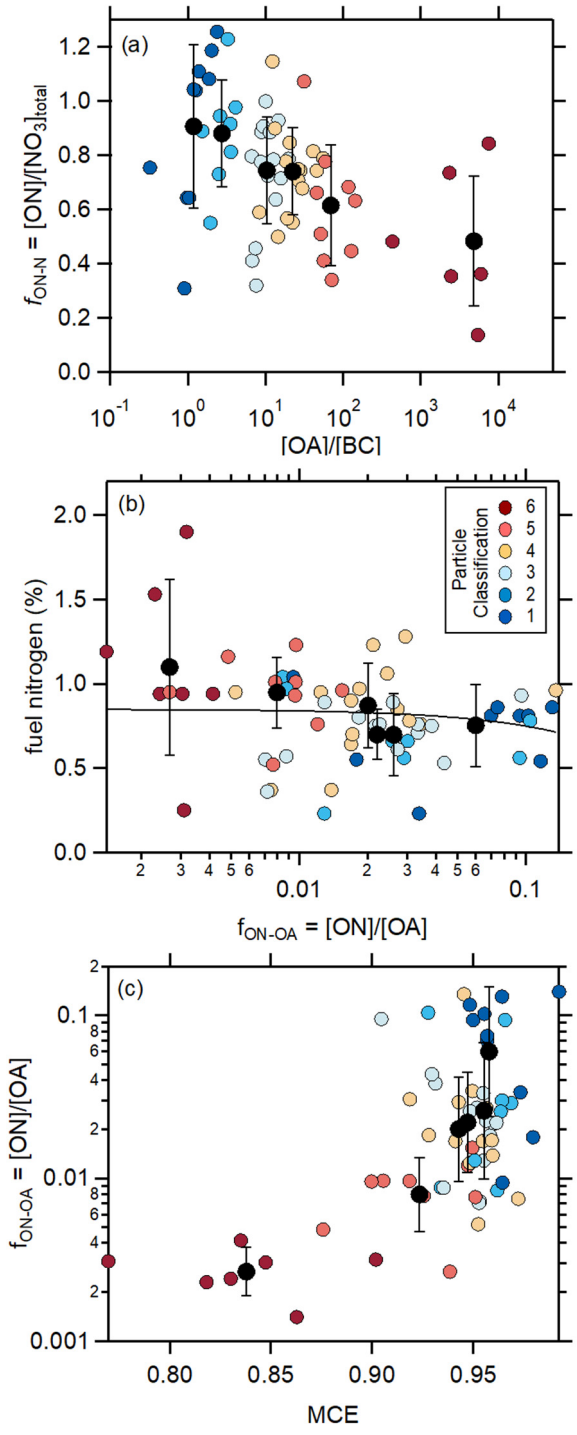

Figure S2. (a) Relationship between fuel nitrogen and the fraction of OA that is organic nitrate, f_{ON-N}. There is no correlation between the two. (b) Relationship between f_{ON-OA} and the modified combustion efficiency, MCE. Results for individual burns are shown as points colored by the particle Class, and Class average values are shown as black circles. Uncertainties on the Class averages are 1σ based on measurement variability.

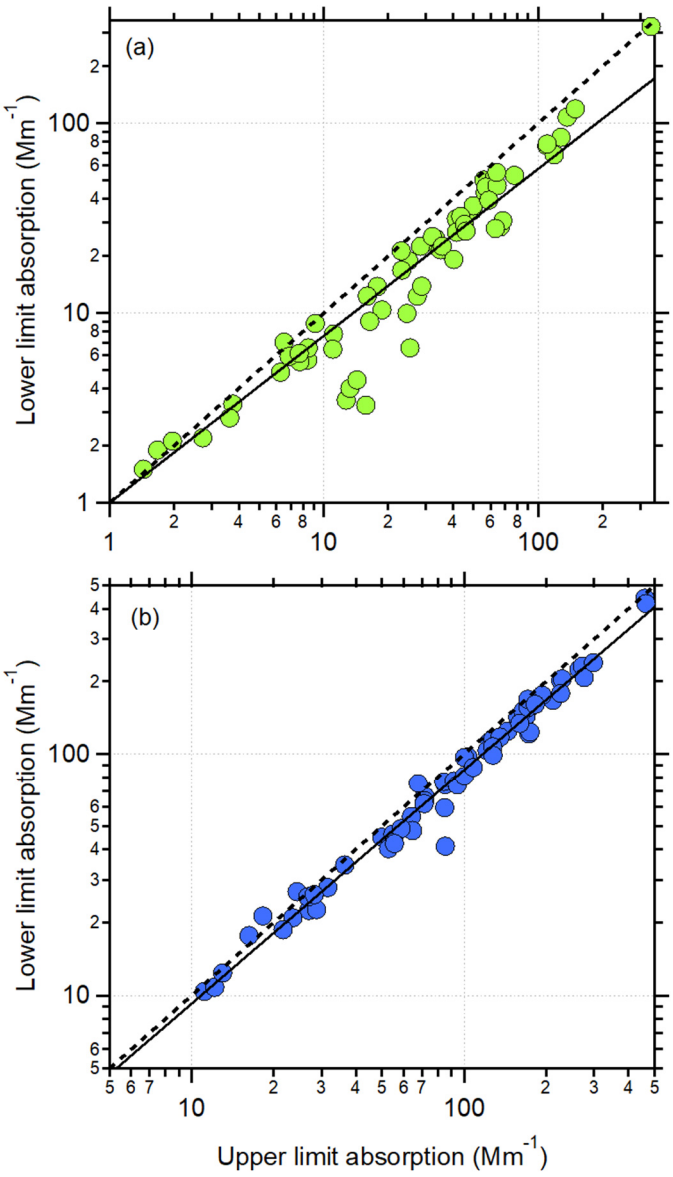

152

153 **Figure S3.** The derived lower limit brown carbon absorption versus the upper limit brown carbon
154 absorption at (a) 532 nm and (b) 405 nm. The lower limit estimate for BrC absorption accounts for
155 the potential influence of coating-induced enhancements. The dashed line is the one-to-one line
156 and the solid line is a linear fit with slopes equaling 0.88 at 532 nm and 0.97 at 405 nm.

157

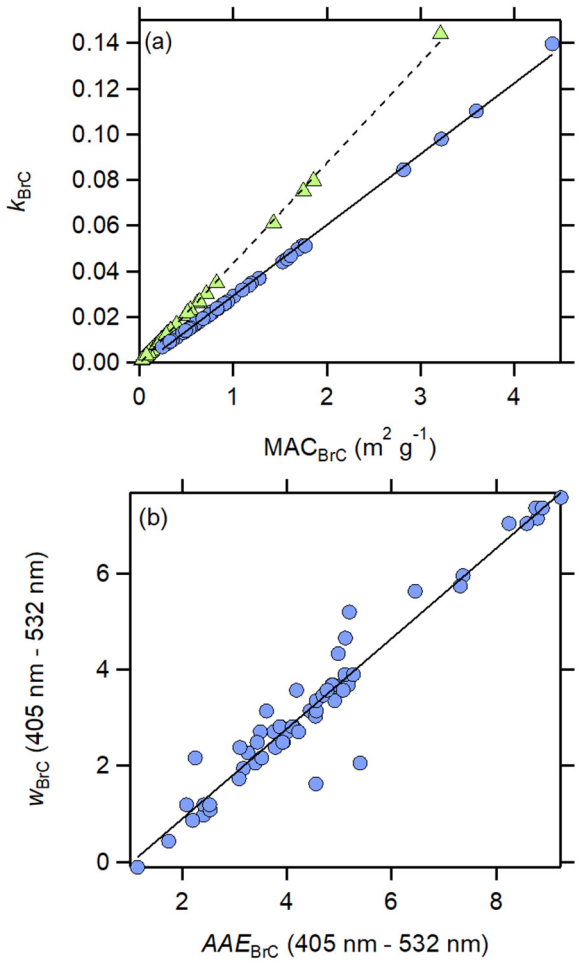

158

159 **Figure S4.** (a) Relationship between the imaginary refractive index for BrC, k_{BrC}, at 405 nm (blue
160 circles) and the observed MAC_{BrC} at 405 nm or at 532 nm (green triangles). Lines are linear fits to
161 the observations. (b) Relationship between the wavelength dependence of k_{BrC}, w_{BrC}, determined
162 for the 405 nm – 532 nm pair, and the AAE_{BrC} for the same wavelengths.
163

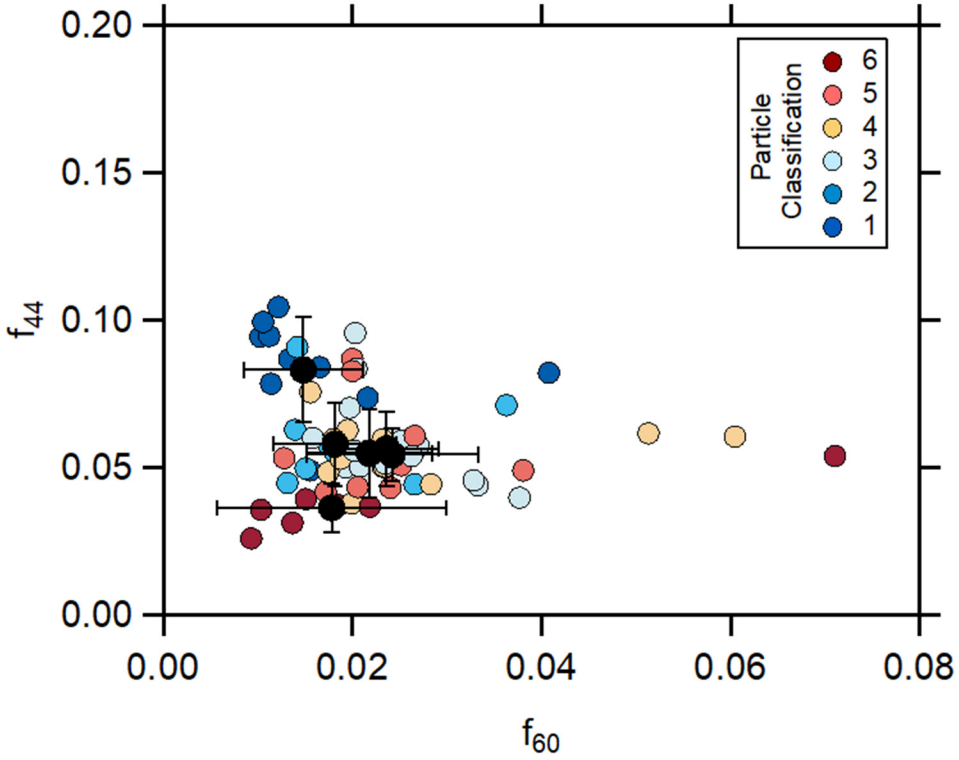

Figure S5. The relationship between the fractional abundance of the m/z = 44 (f_{44}) and m/z = 60 (f_{60}) ions from organic aerosol. Points are colored by particle class for individual burns, and the class averages shown in black.

Table S1. Fuels combusted. Further details regarding fuel properties are available at the NOAA data repository, in particular in the summary spreadsheet (https://esrl.noaa.gov/csd/groups/csd7/measurements/2016firex/FireLab/DataDownload/FIREX_BurnListComplete_V5.xlsx; access date 04 February 2019)

Fuel Type
Bear Grass
Building Material - Untreated Wood
Ceanothos
Chapparral (canopy)
Chamise
Manzanita
Douglas Fir (litter, canopy, mixture, rotten log)
Dung
Engelmann spruce (canopy, mixture, duff)
Excelsior (wood wool)
Jeffrey Pine (duff)
Juniper (canopy)
Loblolly pine (litter)
Lodgepole (canopy, litter, mixture)
Peat
Ponderosa pine (litter, canopy, mixture, rotten log)
Rice Straw, Arkansas
Sage
Sage Brush
Subalpine fir (canopy, litter, mix, duff)

Table S2. Fit coefficients for the various fits performed, organized by fit type (e.g. sigmoidal, power law, linear, exponential). Note: continues on second page.

y	x	c_1	c_2	c_3	c_4	r^2
	$y = c_1 + \frac{c_2}{1 + \frac{\exp(c_3 - x)}{c_4}}$					
SSA_{405nm}	log([OA]/[BC])	0.03	0.93	0.444	0.579	
SSA_{532nm}	log([OA]/[BC])	0.085	0.91	0.623	0.520	
SSA_{781nm}	log([OA]/[BC])	0.10	0.90	0.700	0.538	
$AAE_{405\text{-}532}$	log([OA]/[BC])	1.25	7.81	2.298	0.554	
$\log(MAC_{BC,405nm})$	log([OA]/[BC])	1.072	2.94	2.914	0.765	
$\log(MAC_{BC,532nm})$	log([OA]/[BC])	0.94	2.56	3.721	0.900	
$\log(MAC_{BC,781nm})$	log([OA]/[BC])	0.74	1.62	3.411	0.655	
$\log(f_{OA,int})$	log([OA]/[BC])	0	-2.43	1.477	0.987	
$\log(R_{OA,BC})$	log([OA]/[BC])	-1.76	3.70	0.462	1.823	
$\log(MAC_{BrC,405nm})$	log([OA]/[BC])	1.072	-1.519	0.053	0.732	
AAE_{405nm}	MCE	9.124	-7.476	0.884	0.0236	
AAE_{405nm}	MCE*	9.723	-13.142	0.932	0.0452	
$\log(MAC_{BC,405nm})$	MCE	3.523	-2.251	0.874	0.0198	
$\log(MAC_{BC,405nm})$	MCE*	4.949	-5.073	0.882	0.0705	
log([OA]/[BC])	MCE*	4.030	-39.57	1.072	0.0500	
	$y = c_1 + c_2 \cdot x^{c_3}$					
SSA_{405nm}	MCE	0.954	-0.880	22.76		
SSA_{405nm}	MCE*	0.939	-26.34	88.29		
log([OA]/[BC])	MCE	7.952	-8.272	3.351		
	$y = c_1 \cdot x + c_2$					
f_{44}	log([OA]/[BC])	-0.0097	0.0686			0.33
O:C	log([OA]/[BC])	-0.0345	0.407			0.17
H:C	log([OA]/[BC])	0.0228	1.737			0.27
$\log(MAC_{BrC,405nm})$	$\log(f_{ON\text{-}OA})$	0.322	0.446			0.33
$\log(MAC_{BrC,405nm})$	$\log(f_{ON\text{-}OA})^*$	0.856	0.538			0.81
$\log(MAC_{BrC,405nm})$	f_{60}/f_{44}	-0.396	0.043			0.11
$\log(MAC_{BrC,405nm})$	f_{60}/f_{44}^*	-2.242	0.803			0.96
log([ON]/[OA])	log([OA]/[BC])	-1.342	-0.320			0.47
log([ON]/[OA])	log([OA]/[BC])*	-1.342	-0.320			0.47
$k_{BrC,405nm}$	$MAC_{BrC,405nm}$	0.03104	-0.00177			0.99
$k_{BrC,532nm}$	$MAC_{BrC,532nm}$	0.0440	-0.00048			0.99

y	x	c_1	c_2	c_3	c_4	r^2
$w_{BrC,405-532}$	$AAE_{BrC,405-532}$	0.938	0.976			0.96
	$y = c_1 + c_2 \cdot \exp(-c_3 \cdot x)$					
MFR_{OA}	log([OA]/[BC])	0.00175	0.1760	0.8520		0.157

* Fits were performed to the Class averages, rather than to the individual burns.

178

179

Table S3. Literature imaginary refractive index and *MAC* values for biomass burning derived brown carbon.

	λ , nm	k_{BBOA}	MAC_{BBOA} $m^2\ g^{-1}$	Optical Measurement	Aerosol type sampled	Sampling Location	Literature
Laboratory	550	0.02-0.06		Aethalometer	Oak burning POA	-	(Saleh et al., 2013)
	550	0.015-0.04		Aethalometer	Pocosin Pine burning POA	-	(Saleh et al., 2013)
	550	0.0055-0.022		Aethalometer	Galberry burning POA	-	(Saleh et al., 2013)
	400	0.038	1.1	UV/Vis (filter methanol extracts)	Pine/Oak wood burning	-	(Chen and Bond, 2010)
	405	0.015		Photo-Acoustic Spectrometer	Tar balls from Ponderosa Pine Duff burning	-	(Chakrabarty et al., 2010)
	405	0.0076		Photo-Acoustic Spectrometer	Tar balls from Alaskan Duff burning	-	(Chakrabarty et al., 2010)
	550		0.8-3.2	CLAP	Tar balls from liquid tar (turkey oak)	-	(Hoffer et al., 2016)
	405	0.01	0.35	Photo-Acoustic Spectrometer	Alaskan Peat	-	(Sumlin et al., 2017)
Ambient	404	0.01	1.0-1.1	Photo-Acoustic Spectrometer	Wild fire, near-source emission	Four Mile Canyon, Colorado	(Lack et al., 2012a)
	470		1.01	Aethalometer	Biomass burning influenced	Beijing, China	(Yang et al., 2009)
	400	0.112	2.9	Filter transmission	Wood burning and biomass smoke aerosols	Savanna	(Kirchstetter et al., 2004)
	532	0.0016-0.0019	0.029-0.031	Photo-Acoustic Spectrometer	HULIS from biomass burning aerosols	Amazon basin	(Hoffer et al., 2006)
	Broadband	0.05-0.07		Airborne lidar	Upwind of forest fires	Northern Canada	(Wandinger et al., 2002)
	Broadband	0.07±0.03/ 0.04±0.01		White light optical particle counter	Open fire/ Smoldering phase	Urban Rehovot, Israel	(Adler et al., 2011)
	405	0.037	0.79 or 1.22	Photo-Acoustic Spectrometer	Residential biomass burning influenced	Fresno, CA	(Zhang et al., 2016)
	405		0.84	Photo-Acoustic Spectrometer	Residential biomass burning influenced	Fresno, CA	(Cappa et al., 2019b)
	405		2.3	Aethelometer	Biomass burning influenced	Guangzhou, China	(Qin et al., 2018)
	365		0.32	Water soluble organic carbon	Plume intercept – closest point to fire	Western US	(Forrister et al., 2015)
	365		1.35	Water soluble organic carbon	Regional biomass burning	SE US	(Washenfelder et al., 2015)
	405	0.037		Water soluble organic carbon	Regional	Kanpur, India	(Shamjad et al., 2016)
	405		0.7-1.3	Water soluble organic carbon	Bonfire festival	Rehovot, Israel	(Bluvshtein et al., 2017)
	405		0.6	Methanol soluble organic carbon	Prescribed burn	NW US	(Xie et al., 2017)